nature geoscience

LETTERS

PUBLISHED ONLINE: 16 JANUARY 2011 | DOI: 10.1038/NGEO1062

# Radiative forcing and albedo feedback from the Northern Hemisphere cryosphere between 1979 and 2008

M. G. Flanner[1]*, K. M. Shell[2], M. Barlage[3], D. K. Perovich[4] and M. A. Tschudi[5]

**The extent of snow cover[1] and sea ice[2] in the Northern Hemisphere has declined since 1979, coincident with hemispheric warming and indicative of a positive feedback of surface reflectivity on climate. This albedo feedback of snow on land has been quantified from observations at seasonal timescales[3–6], and century-scale feedback has been assessed using climate models[7–10]. However, the total impact of the cryosphere on radiative forcing and albedo feedback has yet to be determined from measurements. Here we assess the influence of the Northern Hemisphere cryosphere on Earth's radiation budget at the top of the atmosphere—termed cryosphere radiative forcing—by synthesizing a variety of remote sensing and field measurements. We estimate mean Northern Hemisphere forcing at −4.6 to −2.2 W m$^{-2}$, with a peak in May of −9.0 ± 2.7 W m$^{-2}$. We find that cyrospheric cooling declined by 0.45 W m$^{-2}$ from 1979 to 2008, with nearly equal contributions from changes in land snow cover and sea ice. On the basis of these observations, we conclude that the albedo feedback from the Northern Hemisphere cryosphere falls between 0.3 and 1.1 W m$^{-2}$ K$^{-1}$, substantially larger than comparable estimates obtained from 18 climate models.**

Climate feedback mechanisms are often characterized in terms of their influence on top-of-atmosphere (TOA) net energy flux ($F$) with changing surface temperature[7–10], highlighting the utility of understanding the direct impact of evolving Earth System components on $F$. Extending a previous analysis of seasonal snow radiative effect[3], we define cryosphere radiative forcing (CrRF) as the instantaneous perturbation to Earth's TOA energy balance induced by the presence of surface cryospheric components. CrRF is thus directly analogous to cloud radiative forcing, a commonly used diagnostic in climate model and remote sensing analyses. This study focuses entirely on the short-wave (solar spectrum) component of Northern Hemisphere CrRF. Long-wave CrRF may be non-negligible in regions where snow or ice alters surface emissivity[3], and long-wave feedbacks associated with cryosphere evolution can also be large[11].

CrRF is influenced by several factors, including the surface albedo change induced by snow or ice, which depends on snow/ice albedo and characteristics of the snow-free surface (especially vegetation), and local insolation and atmospheric state (primarily cloudiness), which determine the propagation of surface albedo changes to TOA flux[8,12]. Here, we quantify plausible CrRF ranges by combining observations of snow and sea-ice cover fraction ($S_x$, where $x$ indicates snow or sea ice), surface albedo contrast between snow/ice-covered and snow/ice-free surfaces ($\Delta\alpha_x$), and TOA flux variation with surface albedo change ($\partial F/\partial\alpha$). Our bottom-up approach offers an independent assessment of land CrRF determined directly from TOA fluxes[3] and the potential of attributing observed TOA flux variability[13] to cryospheric evolution.

Time ($t$)-dependent CrRF, measured in watts per square metre (W m$^{-2}$), within a region $R$ (here, the Northern Hemisphere) of area $A$, composed of gridcells $r$ can be represented as:

$$\mathrm{CrRF}(t,R) = \frac{1}{A(R)} \int_R S_x(t,r)\, \frac{\partial\alpha}{\partial S_x}(t,r)\, \frac{\partial F}{\partial\alpha}(t,r)\, dA(r) \qquad (1)$$

Here, we assume that (monthly and spatially varying) $\partial\alpha/\partial S_x$ and $\partial F/\partial\alpha$ are constant with $S_x$ and $\alpha$, respectively, and replace $\partial\alpha/\partial S_x$ with mean albedo contrast ($\Delta\alpha_x$) observations that are specific to the applied snow/ice cover data. We use 1979–2008 monthly gridded binary snow cover[14] and sea-ice concentration[15] derived, respectively, from visible and microwave remote sensing. We derive monthly climatologies of $\Delta\alpha_{\mathrm{snow}}$ (Supplementary Figs S1 and S2) from 2000 to 2008 Moderate Resolution Imaging Spectroradiometer (MODIS) observations and coincident (binary) snow cover, filled with annual-mean MODIS or 1982–2004 Advanced Polar Pathfinder (APP-x) monthly albedo data[16]. We partition sea ice into multi-year (MYI) and first-year (FYI) concentrations[17,18] and apply to each ice type monthly varying $\Delta\alpha_{\mathrm{ice}}$ functions (Supplementary Fig S3) derived from field measurements[19] and remote sensing of FYI parcels[20].

To characterize uncertainty, we apply minimum, central and maximum estimates of $\Delta\alpha$, combined with six $\partial F/\partial\alpha$ products, producing 18 scenarios of the time variation and trend of CrRF from 1979 to 2008. Ranges of $\Delta\alpha_{\mathrm{snow}}$ and $\Delta\alpha_{\mathrm{ice}}$ are determined, respectively, from albedo variance of different land classes[21] (Supplementary Table S1) and from extensive field measurements[19] (Supplementary Fig S3). We apply spatially and monthly varying (annually repeating) $\partial F/\partial\alpha$ 'radiative kernel' data sets created previously[9,10] from the Community Atmosphere Model (CAM3) of the National Center for Atmospheric Research and the Atmosphere Model 2 (AM2) of the Geophysical Fluid Dynamics Laboratory, and we derive two annually varying $\partial F/\partial\alpha$ kernels using radiative transfer modelling with cloud fraction and optical depth data from the International Satellite Cloud Climatology Project[22] (ISCCP-D2), and APP-x (ref. 16). We also include clear-sky $\partial F/\partial\alpha$ products[9,10]

[1]Department of Atmospheric, Oceanic and Space Sciences, University of Michigan, Ann Arbor Michigan 48109, USA, [2]College of Oceanic and Atmospheric Sciences, Oregon State University, Corvallis, Oregon 97331, USA, [3]National Center for Atmospheric Research, Boulder, Colorado 80307, USA, [4]Cold Regions Research and Engineering Laboratory, US Army Engineer Research and Development Center, Hanover, New Hampshire 03755, USA, [5]Colorado Center for Astrodynamics Research, University of Colorado, Boulder, Colorado 80309, USA. *e-mail: flanner@umich.edu.

**Table 1 | Northern Hemisphere CrRF, in W m$^{-2}$, averaged over 1979–2008 for all albedo contrast and radiative kernel combinations.**

| Kernel ($\partial F/\partial\alpha$) | Albedo contrast ($\Delta\alpha$) | | |
|---|---|---|---|
| | Low | Central | High |
| CAM3 | −2.3 (51) | −3.1 (57) | −3.9 (61) |
| AM2 | −2.7 (52) | −3.6 (59) | −4.4 (63) |
| ISCCP | −2.2 (58) | −3.1 (63) | −4.0 (66) |
| APP-x | −2.6 (55) | −3.6 (61) | −4.6 (63) |
| CAM3 clear-sky | −4.5 (53) | −6.1 (59) | −7.7 (62) |
| AM2 clear-sky | −4.3 (55) | −5.7 (59) | −7.1 (62) |

The numbers in parenthesis indicate the per cent of CrRF caused by land-based snow.

to diagnose the magnitude of cloud damping. All products were remapped to 1° × 1° resolution for analysis. Although these scenarios do not fully span the uncertainty in parameter space, they do provide information on the importance of two key terms in equation (1). The ranges of $\Delta\alpha$ represent our estimate of uncertainty in $\partial\alpha/\partial S$, whereas the different $\partial F/\partial\alpha$ products illustrate the CrRF range produced with different techniques (annually varying or annually repeating atmospheric states) and different modelled and observed atmospheric conditions.

Table 1 lists mean 1979–2008 Northern Hemisphere CrRF from all radiative kernel and albedo contrast scenarios. The mean (full range) of the 12 all-sky cases is −3.3 (−4.6 to −2.2) W m$^{-2}$, of which −2.0 (−2.9 to −1.2) W m$^{-2}$ is from land-based snowpack. All-sky CrRF is about 15% greater with the AM2 and APP-x kernels than with CAM3 and ISCCP kernels. Clear-sky CrRF is −5.9 (−4.3 to −7.7) W m$^{-2}$ indicating that clouds mask slightly less than half of the cryosphere radiative effect[12,23].

Mean annual cycles of land and sea-ice CrRF are shown in Fig. 1a. $CrRF_{snow}$ peaks broadly at about −4.5 W m$^{-2}$ during March–May, when hemispheric insolation and snow cover are both large. $CrRF_{ice}$ peaks at −4.7 ± 1.3 W m$^{-2}$ in May, despite greater June insolation, because of higher pre-melt ice albedo[19] (Supplementary Fig. S3) and greater May ice extent. The Northern Hemisphere reflects to space an additional 9.0 ± 2.7 W m$^{-2}$ during May because of the cryosphere. $CrRF_{snow}$ increases slightly during October–January with increasing snow cover, whereas diminishing polar insolation maintains small $CrRF_{ice}$.

Spatial distributions of annual-mean and seasonal CrRF are shown in Fig. 2a and Supplementary Fig. S5, respectively. Except during winter, CrRF is generally larger over the Arctic Ocean than over land, a consequence of persistent ice cover and large $\Delta\alpha_{ice}$. Sparsely vegetated land blanketed with snow and exposed to intense spring insolation can have greater CrRF than sea ice but, averaged over 1° × 1° areas, $\Delta\alpha_{snow}$ is always reduced by snow patchiness and/or vegetation. CrRF over Greenland is uncertain because of unknown and variable ground albedo beneath the ice sheet. We assume uniform ice-free albedo of 0.26, typical of sparsely vegetated land (Supplementary Table S1).

Changes in Northern Hemisphere CrRF from 1979 to 2008 (ΔCrRF), expressed as linear trends multiplied by the time interval, are listed in Table 2, and all-sky CrRF anomaly time series are shown in Supplementary Fig. S4. The mean (full range) 30-year ΔCrRF of the 12 all-sky cases is +0.45 (0.27–0.72) W m$^{-2}$, to which snow and sea-ice changes contributed almost equally. An analysis of twenty-first-century albedo feedbacks in models contributing to the Climate Model Intercomparison Project[8] (CMIP3) also found similar contributions from snow and sea ice. All trends are significant at $P = 0.01$. Interestingly,

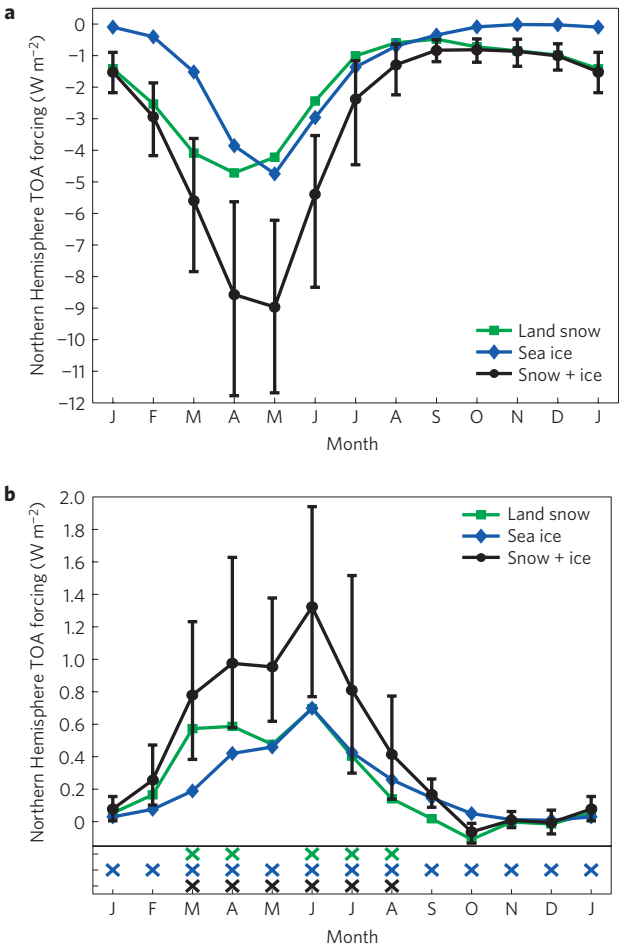


**Figure 1 | Seasonal cycles of Northern Hemisphere CrRF and changes in forcing from 1979 to 2008.** Contributions to TOA forcing for land-based snowpack (green, squares), sea ice (blue, diamonds) and combined snow + sea-ice (black, circles). **a**, The mean influence of the cryosphere during 1979–2008. **b**, 30-year changes calculated from linear trends. The whiskers depict full ranges of snow + sea-ice cryosphere forcing from the 12 all-sky albedo contrast and radiative kernel scenarios listed in Tables 1 and 2. The crosses in **b** indicate months of statistically significant change at $P = 0.01$.

changes are largest with the ISCCP and APP-x kernels, which exhibit mean CrRF similar to the model kernels. One explanation for greater ΔCrRF with annually varying, coincident cloud conditions is that cloud evolution amplified cryosphere-induced radiative anomalies. Qualitative evidence for such amplification comes from a study of surface-based cloud observations in the Arctic Ocean[24]. Our ability to assess cloud feedback is limited, however, by the monthly resolution and temporal extent of the data and by large uncertainty in cloud retrievals over the Arctic. Research with higher fidelity radar and lidar products shows that cloud cover may increase over regions of fresh sea-ice loss during autumn, but not summer[25]. As cloud changes alter CrRF (even with constant snow/ice cover), a more straightforward interpretation of ΔCrRF comes from the annually constant model kernels, which show similar ΔCrRF in spite of different base albedo, clouds, aerosols and water vapour. The mean ΔCrRF obtained with annually repeating cloud conditions (conducted for each year of cloud data) from the ISCCP and APP-x data sets is, respectively, 0.50 and 0.59 W m$^{-2}$. Thus, the observational kernels produce greater ΔCrRF even without temporally coincident cloud evolution. We suggest a

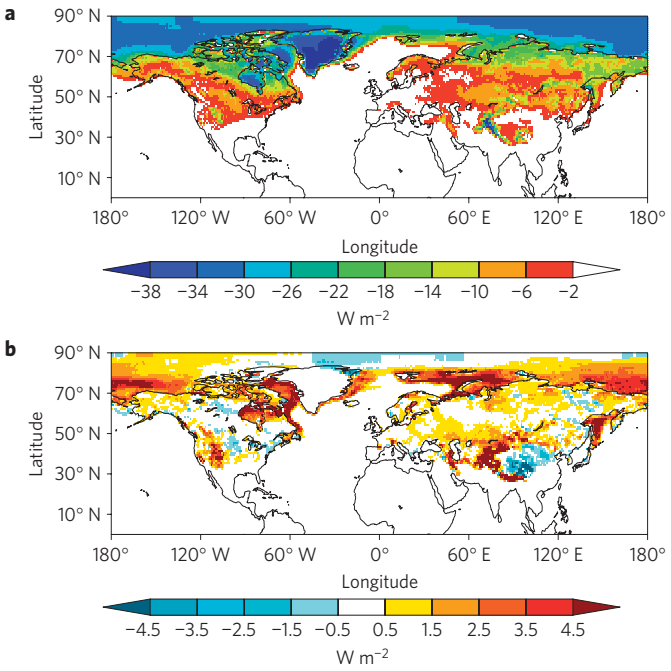


**Figure 2 | Annual-mean CrRF and change in CrRF from 1979 to 2008.** **a**, The mean influence of the cryosphere during 1979–2008. **b**, Thirty-year changes calculated from linear trends. Negative cryosphere forcing in **a** indicates that snow and ice decrease the net TOA solar energy flux, and positive changes in **b** indicate that the cryospheric cooling effect has decreased since 1979. These data were derived with central estimates of albedo contrast and the CAM3 radiative kernel[9]. Thirty-year changes in **b** were derived from linear trend analysis at each gridcell.

central range of 0.38–0.59 $W\,m^{-2}$ for ΔCrRF with annually repeating cloud conditions.

Maximum (minimum) $\Delta\alpha_{snow}$ and $\Delta\alpha_{ice}$ scenarios increase (decrease) their respective all-sky CrRF by 31% (34%) and 15% (15%), whereas variability across kernels is smaller. Previous work found that $\Delta\alpha$ is a greater source of variability than $\partial F/\partial\alpha$ in determining snow feedback strengths within CMIP3 models[5,8]. Variability in our estimates is greater for land than sea ice, which follows from large snow-covered albedo variability caused by heterogeneous vegetation and orography[21] (Supplementary Fig. S1). The largest $\Delta\alpha_{snow}$ variability occurs over shrublands, grasslands and sparsely vegetated terrain (Supplementary Table S1). Although pre-melt sea-ice albedo varies little because of snow cover[19], melt-season albedo also becomes quite variable (Supplementary Fig. S3) and depends on ice thickness, pond area and depth[19], bubble and ice grain size, and content of sediment, algae and light-absorbing impurities. We account for this variability implicitly, through liberal $\Delta\alpha_{ice}$ ranges, and acknowledge that a more constrained assessment could be produced with improved knowledge of the ice state. This study differentiates only between MYI and FYI, the latter of which is darker because of greater morphological susceptibility to ponding and tendency to be thinner. The range of $\Delta\alpha_{ice}$ represents variability observed along a line that included a variety of ponded, bare and snow-covered ice[19]. These June–September albedos are, however, ~15% lower than 40-year means measured at a Soviet drifting station[19], illuminating a potential source of low bias in our $CrRF_{ice}$ estimates.

Figure 2b and Supplementary Fig. S6 show spatial distributions of annual-mean and seasonal ΔCrRF with the CAM3 kernel. ΔCrRF is large and positive over Eurasian land during March–May and over much of the Arctic Ocean during June–August. Autumn

**Table 2 | Change in Northern Hemisphere CrRF, in $W\,m^{-2}$, from 1979 to 2008 for all albedo contrast and radiative kernel combinations.**

| Kernel ($\partial F/\partial\alpha$) | Albedo contrast ($\Delta\alpha$) | | |
|---|---|---|---|
| | Low | Central | High |
| CAM3 | +0.26 (42) | +0.38 (50) | +0.48 (53) |
| AM2 | +0.29 (41) | +0.40 (49) | +0.49 (52) |
| ISCCP | +0.40 (48) | +0.57 (54) | +0.72 (56) |
| APP-x | +0.31 (41) | +0.48 (49) | +0.59 (49) |
| CAM3 clear-sky | +0.58 (38) | +0.82 (45) | +1.00 (48) |
| AM2 clear-sky | +0.58 (41) | +0.77 (46) | +0.97 (49) |

The numbers in parenthesis indicate the per cent of change due to land-based snow.

anomalies are large in the Chukchi Sea, where September ice has diminished[2]. Large portions of North America and Eurasia show slightly negative ΔCrRF during September–November, associated with increased snow cover[1].

Thirty-year ΔCrRF by month is depicted in Fig. 1b. Sea-ice ΔCrRF peaks distinctly in June, with a smooth seasonal cycle. Thus, although sea-ice loss has been largest in September[2], April–August ice changes, facilitated by stronger insolation, have driven greater change in $CrRF_{ice}$. $\Delta CrRF_{snow}$ is statistically significant ($P = 0.01$) during March–April and June–August, whereas $\Delta CrRF_{ice}$ is significant in all months (although very small during winter). Our technique distinguishes between FYI and MYI and thus includes changes in CrRF caused by ice age changes, in addition to the dominant influence of ice concentration changes. We estimate that 14% of $\Delta CrRF_{ice}$ was caused by transitions from MYI to FYI. A weakness of our approach, however, is applying fixed annual cycles of FYI and MYI albedo, meaning we neglect contributions to $\Delta CrRF_{ice}$ of altered sea-ice albedo associated with, for example, changes in timing of melt onset and freeze-up. Sea-ice-absorbed solar flux is especially sensitive to timing of melt onset, which decreases albedo coincidentally with near-maximal insolation. At one site, melt onset ranged by 16 days over six years[26], and it has become earlier by about 8 days over the Arctic Ocean since 1979 (ref. 27). Fixed $\Delta\alpha_{snow}$ cycles similarly fail to capture interannual changes in albedo of snow-covered regions (for example, as caused by altered snow metamorphism, vegetation or aerosol deposition)[6,23]. If snow has darkened with warmer spring temperatures in recent years, ΔCrRF estimates would be further biased low. In addition, we show no change in CrRF over Greenland (Fig. 2b), but melt area has increased significantly since 1979 (ref. 28), contributing to some decrease in albedo. We discuss other potential sources of bias and comparisons with previous analyses in the Supplementary Information.

Estimates of 1979–2008 NH warming obtained from the GISS Surface Temperature Analysis[29] and Hadley Centre/Climate Research Unit HadCRUT3v dataset[30] are 0.79 and 0.67 °C, respectively. Ranges of ΔCrRF combined with these warmings yield NH cryosphere albedo feedback ($\Delta F_{cryo}/\Delta T_s$) of 0.62 (0.33–1.07) $W\,m^{-2}\,K^{-1}$, where the range indicates the extreme minimum/maximum combinations of $\Delta T$ and ΔCrRF (Table 2). Using models from the CMIP3 multi-model dataset, we quantify a 1980–2010 NH model feedback of only $0.25 \pm 0.17\,W\,m^{-2}\,K^{-1}$. The large range is probably due to the spread of albedo feedbacks in climate models and the relatively short period of differencing. This discrepancy with our estimate indicates that either other surface processes are driving negative albedo feedback in models that offset strong cryosphere feedback, or the cryosphere is responding more sensitively to, and driving stronger climate warming than models indicate. Future analyses can provide

information on the relative importance of the two possibilities. In support of the latter, recent work determined that Northern Hemisphere sea ice is declining faster than models simulate[31]. Although 30-year feedback strengths may be strongly affected by climate variability, we believe our range provides a conservative lower bound on the present feedback because of $\Delta$CrRF biases described earlier. Thus, we conclude that CMIP3 models probably underestimate the recent surface albedo feedback. In summary, these estimates of CrRF evolution will help ascribe causes of observed increases and variability in net TOA solar flux[13], evaluate model cryosphere processes and constrain one determinant of Earth's climate sensitivity.

## Methods

We use monthly binary snow cover data (89 × 89 gridcells, projected on a polar stereographic grid) from the National Oceanic and Atmospheric Administration (NOAA), maintained by Rutgers University[14] (http://climate.rutgers.edu/snowcover), and derived from Advanced Very High Resolution Radiometer observations. We use monthly gridded sea-ice concentrations derived from microwave retrievals with the NASA Team algorithm[15] and fill the pole-centred data void using a nearest-neighbour algorithm.

We derive land albedo contrast primarily from the MODIS MCD43C3 collection 5 data set (0.05° × 0.05° resolution). We determine monthly snow-covered albedo climatologies of all NOAA/Rutgers gridcells defined binarily as snow-covered at any time during 1979–2008 using the following priority of filling: (1) monthly resolved mean MODIS white-sky albedo of all coincident times during 2000–2008 when at least 50% of the 'snow-covered' gridcell is defined with quality flag 2 or better, (2) annual-mean (quality-filtered) MODIS albedo, averaged only during times of snow cover, (3–4) methods (1) and (2) repeated with 1982–2004 APP-x albedo data[16], which has greater temporal overlap with NOAA/Rutgers snow cover, but which has limited mid-latitude spatial coverage and is derived from lower fidelity observations, and (5) annual-mean MODIS snow-covered albedo by land classification (Supplementary Table S1), defined with University of Maryland/MODIS land cover product MCD12C1. We derive a similar data set using APP-x priority over MODIS (that is, filling priority order 3, 4, 1, 2, 5), but find that it changes our CrRF and $\Delta$CrRF estimates by less than 3%. Furthermore, using only method 5, we obtain CrRF and $\Delta$CrRF estimates that differ by only 3% from the methods described above. We determine monthly resolved snow-free albedo entirely from MODIS product MCD43C3, using its accompanying snow-cover filter and quality flag for strict prevention of snow contamination. Central estimates of $\mathrm{CrRF_{snow}}$ and $\Delta\mathrm{CrRF_{snow}}$ increased very slightly (3% and 2%, respectively) when we applied MODIS black-sky albedo instead of white-sky albedo. We derive maximum/minimum estimates of $\Delta\alpha_{\mathrm{snow}}$ (Supplementary Fig. S2) by adding/subtracting the combined standard deviations of snow-free and snow-covered albedos grouped by land classification (Supplementary Table S1). These mean snow-covered albedos are lower than maximum snow-covered albedos[21] because they are averaged over NOAA/Rutgers gridcells that are partially snow-free. Thus, our $\Delta\alpha_{\mathrm{snow}}$ range includes variability caused by both unresolved snow cover variability within the binary snow product, and variability in the influence of vegetation (within each land class) on albedo contrast.

Sea-ice concentrations were partitioned into FYI and MYI using ice motion vectors derived from microwave and Advanced Very High Resolution Radiometer remote sensing products, combined with Lagrangian parcel tracking at weekly resolution[17,18]. We use seasonally dependent ranges of MYI albedo derived from ground measurements over heterogeneous ice terrain (snow-covered ice, various morphologies of bare ice, and ponded ice)[19], and derive FYI albedo from unpublished ground measurements made by D.K.P. during April–June, and APP-x albedo[16] averaged over FYI parcels determined with the Lagrangian tracking method during July–September[20]. Lacking reliable statistics on FYI albedo variability, we apply the MYI albedo variance to FYI (Supplementary Fig. S3). Winter values are filled with typical snow-covered ice albedo and have negligible impact on solar CrRF. Although open-water albedo can vary slightly, depending, for example, on solar angle and phytoplankton content, we assume a constant value of 0.07 (ref. 19).

We derive annually varying estimates of $\partial F/\partial\alpha$ using 1984–2008 2.5° × 2.5° resolution ISCCP-D2 (ref. 22) and 1982–2004 25 × 25 km resolution APP-x (ref. 16) cloud optical depth, filled with mean annual cycles to achieve continuous 1979–2008 data, and ISCCP-D2 cloud fractions for weighting with clear-sky fluxes. We prescribe these properties, along with 0.01 perturbations to surface albedo[9,10], in a radiative transfer model[32] with profiles of atmospheric gases and aerosols typical of mid-latitude summer and winter, sub-Arctic summer, and tropical environments. Thus, $\partial F/\partial\alpha$ variability caused by gas and aerosol concentration changes is poorly captured in these radiative kernels, although such variability is probably much smaller than that generated by (optically thicker) clouds. The model-derived CAM3 and AM2 monthly $\partial F/\partial\alpha$ products are described elsewhere[9,10].

All products are mapped with conservative area regridding from their native resolutions to 1° × 1° for analysis. Linear trends and statistical significance are determined, respectively, with the Mann–Kendall and Theil–Sen techniques, including trend-free pre-whitening to account for autocorrelation[1].

For the CMIP3 models, we use the CAM3 radiative kernel[9] to determine albedo feedback between years 2001 and 2010 of twenty-first-century Special Report on Emissions Scenario A1B simulations and years 1981–1990 simulated by the same model, but for the twentieth-century case. The 18 models used are listed in Supplementary Table S2. The feedback calculation technique requires a multi-year average, and the time period considered is short. Using ten years offers a compromise between maximizing the climate change signal and reducing noise from natural climate variability. We use 2001–2010 rather than 1999–2008 for simplicity because the Special Report on Emissions Scenario A1B scenarios start at year 2000. The specific start date is unlikely to alter the feedback estimates.

Received 13 August 2010; accepted 8 December 2010; published online 16 January 2011

## References


1. Déry, S. J. & Brown, R. D. Recent Northern Hemisphere snow cover extent trends and implications for the snow-albedo-feedback. *Geophys. Res. Lett.* **34,** L22504 (2007).
2. Serreze, M. C., Holland, M. M. & Stroeve, J. Perspectives on the Arctic's shrinking sea-ice cover. *Science* **315,** 1533–1536 (2007).
3. Groisman, P. Y., Karl, T. R. & Knight, R. W. Observed impact of snow cover on the heat balance and the rise of continental spring temperatures. *Science* **263,** 198–200 (1994).
4. Hall, A. & Qu, X. Using the current seasonal cycle to constrain snow albedo feedback in future climate change. *Geophys. Res. Lett.* **33,** L03502 (2006).
5. Qu, X. & Hall, A. Assessing snow albedo feedback in simulated climate change. *J. Clim.* **19,** 2617–2630 (2006).
6. Fernandes, R. *et al.* Controls on Northern Hemisphere snow albedo feedback quantified using satellite earth observations. *Geophys. Res. Lett.* **36,** L21702 (2009).
7. Colman, R. A comparison of climate feedbacks in general circulation models. *Clim. Dyn.* **20,** 865–873 (2003).
8. Winton, M. Surface albedo feedback estimates for the AR4 climate models. *J. Clim.* **19,** 359–365 (2006).
9. Shell, K. M., Kiehl, J. T. & Shields, C. A. Using the radiative kernel technique to calculate climate feedbacks in NCAR's community atmospheric model. *J. Clim.* **21,** 2269–2282 (2008).
10. Soden, B. J. *et al.* Quantifying climate feedbacks using radiative kernels. *J. Clim.* **21,** 3504–3520 (2008).
11. Trenberth, K. E. & Fasullo, J. T. Global warming due to increasing absorbed solar radiation. *Geophys. Res. Lett.* **36,** L07706 (2009).
12. Qu, X. & Hall, A. Surface contribution to planetary albedo variability in cryosphere regions. *J. Clim.* **18,** 5239–5252 (2005).
13. Wielicki, B. A. *et al.* Changes in Earth's albedo measured by satellite. *Science* **308,** 825 (2005).
14. Robinson, D. A. & Frei, A. Seasonal variability of Northern Hemisphere snow extent using visible satellite data. *Professional Geogr.* **51,** 307–314 (2000).
15. Cavalieri, D., Parkinson, C., Gloersen, P. & Zwally, H. J. Sea ice concentrations from Nimbus-7 SMMR and DMSP SSM/I passive microwave data, [1979–2008] (1996, updated 2008). Boulder, CO, USA: National Snow and Ice Data Center. Digital media.
16. Wang, X. & Key, J. R. Arctic surface, cloud, and radiation properties based on the AVHRR polar pathfinder dataset. Part I: Spatial and temporal characteristics. *J. Clim.* **18,** 2558–2574 (2005).
17. Fowler, C., Emery, W. J. & Maslanik, J. Satellite-derived evolution of Arctic sea ice age: October 1978 to March 2003. *IEEE Geosci. Remote Sens. Lett.* **1,** 71–74 (2004).
18. Maslanik, J. A. *et al.* A younger, thinner Arctic ice cover: Increased potential for rapid, extensive sea-ice loss. *Geophys. Res. Lett.* **34,** L24501 (2007).
19. Perovich, D. K., Grenfell, T. C., Light, B. & Hobbs, P. V. Seasonal evolution of the albedo of multiyear Arctic sea ice. *J. Geophys. Res.* **107,** 8044 (2002).
20. Tschudi, M. A., Fowler, C., Maslanik, J. A. & Stroeve, J. Tracking the movement and changing surface characteristics of Arctic sea ice. *IEEE J. Sel. Top. Earth Obs. Remote Sens.* **3,** 536–540 (2010).
21. Barlage, M., Zeng, X., Wei, H. & Mitchell, K. E. A global 0.05° maximum albedo dataset of snow-covered land based on MODIS observations. *Geophys. Res. Lett.* **32,** L17405 (2005).
22. Rossow, W. & Schiffer, R. Advances in understanding clouds from ISCCP. *Bull. Am. Meteorol. Soc.* **80,** 2261–2288 (1999).
23. Qu, X. & Hall, A. What controls the strength of snow-albedo feedback? *J. Clim.* **20,** 3971–3981 (2007).
24. Eastman, R. & Warren, S. Interannual variations of Arctic cloud types in relation to sea ice. *J. Clim.* **23,** 4216–4232 (2010).
25. Kay, J. E. & Gettelman, A. Cloud influence on and response to seasonal arctic sea ice loss. *J. Geophys. Res.* **114,** D18204 (2009).

26. Perovich, D. K., Nghiem, S. V., Markus, T. & Schweiger, A. Seasonal evolution and interannual variability of the local solar energy absorbed by the arctic sea ice–ocean system. *J. Geophys. Res.* **112,** C03005 (2007).
27. Markus, T., Stroeve, J. C. & Miller, J. Recent changes in arctic sea ice melt onset, freezeup, and melt season length. *J. Geophys. Res.* **114,** C12024 (2009).
28. Mote, T. L. Greenland surface melt trends 1973–2007: Evidence of a large increase in 2007. *Geophys. Res. Lett.* **34,** L22507 (2007).
29. Hansen, J., Ruedy, R., Sato, M. & Lo, K. Global surface temperature change. *Rev. Geophys.* **48,** RG4004 (2010).
30. Brohan, P., Kennedy, J. J., Harris, I., Tett, S. F. B. & Jones, P. D. Uncertainty estimates in regional and global observed temperature changes: a new dataset from 1850. *J. Geophys. Res.* **111,** D12106 (2006).
31. Stroeve, J., Holland, M. M., Meier, W., Scambos, T. & Serreze, M. Arctic sea ice decline: Faster than forecast. *Geophys. Res. Lett.* **34,** L09501 (2007).
32. Zender, C. S. *et al*. Atmospheric absorption during the atmospheric radiation measurement (ARM) enhanced shortwave experiment (ARESE). *J. Geophys. Res.* **102,** 29901–29915 (1997).

## Acknowledgements

We thank C. Fowler and J. Maslanik for providing multi-year sea-ice data, T. Estilow and M. J. Brodzik for providing snow and sea-ice data and advice, and S. Warren for reviewing the manuscript. MODIS data are distributed by the Land Processes Distributed Active Archive Center, located at the US Geological Survey Earth Resources Observation and Science Center (lpdaac.usgs.gov). The ISCCP D2 data were obtained from the International Satellite Cloud Climatology Project web site (http://isccp.giss.nasa.gov) maintained by the ISCCP research group at NASA Goddard Institute for Space Studies. We acknowledge the modelling groups, the Program for Climate Model Diagnosis and Intercomparison and the WCRP's Working Group on Coupled Modelling for their roles in making available the WCRP CMIP3 multi-model data set. Research was supported by NSF ATM-0852775 (M.G.F.) and ATM-0904092 (K.M.S.).

## Author contributions

M.G.F. wrote the manuscript and combined all data sets to quantify CrRF. K.M.S. provided radiative kernel data, quantified CMIP3 model feedbacks and helped write the manuscript. M.B. provided land snow-covered albedo data. D.K.P. and M.A.T. provided, respectively, field-measured and remote sensing sea-ice albedo data.

## Additional information

The authors declare no competing financial interests. Supplementary information accompanies this paper on www.nature.com/naturegeoscience. Reprints and permissions information is available online at http://npg.nature.com/reprintsandpermissions. Correspondence and requests for materials should be addressed to M.G.F.